nature photonics

ARTICLES

https://doi.org/10.1038/s41566-020-0647-4

Strain-engineered high-responsivity $MoTe_2$ photodetector for silicon photonic integrated circuits

R. Maiti[1], C. Patil[1], M. A. S. R. Saadi[2], T. Xie[1], J. G. Azadani[3], B. Uluutku[2], R. Amin[1], A. F. Briggs[4], M. Miscuglio[1], D. Van Thourhout[5], S. D. Solares[2], T. Low[3], R. Agarwal[6], S. R. Bank[4] and V. J. Sorger[1]✉

In integrated photonics, specific wavelengths such as 1,550 nm are preferred due to low-loss transmission and the availability of optical gain in this spectral region. For chip-based photodetectors, two-dimensional materials bear scientifically and technologically relevant properties such as electrostatic tunability and strong light–matter interactions. However, no efficient photodetector in the telecommunication C-band has been realized with two-dimensional transition metal dichalcogenide materials due to their large optical bandgaps. Here we demonstrate a $MoTe_2$-based photodetector featuring a strong photoresponse (responsivity 0.5 A W^{-1}) operating at 1,550 nm in silicon photonics enabled by strain engineering the two-dimensional material. Non-planarized waveguide structures show a bandgap modulation of 0.2 eV, resulting in a large photoresponse in an otherwise photoinactive medium when unstrained. Unlike graphene-based photodetectors that rely on a gapless band structure, this photodetector shows an approximately 100-fold reduction in dark current, enabling an efficient noise-equivalent power of 90 pW $Hz^{-0.5}$. Such a strain-engineered integrated photodetector provides new opportunities for integrated optoelectronic systems.

Strain engineering of traditional semiconductors such as Si/Ge and III–V can be utilized to enhance the performance of electronic and photonic devices[1–3]. By inducing strain, the electronic band structure can be modified by epitaxial growth techniques and thus positively impact mobility[4,5]. Lowering the dimensionality from bulk crystals to 2D layered films can enable the material to sustain higher amounts of strain. A straightforwards method to achieve strain in 2D nanocrystals is through mechanical deformation by transferring them onto flexible substrates or wrapping them around prepatterned structures[6–9]. Under small (<2%) compressive (tensile) strain, the bandgap increases (decreases) and can even induce a semiconductor-to-metal phase transition (10% for monolayer) in MoS_2 (refs. [10,11]). It was recently shown that 2.3% of uniaxial strain can strongly modulate the bandgap energy (~70 meV) of monolayer $MoTe_2$ and $MoWTe_2$ (ref. [12]). Beyond such pioneering demonstrations, there is, however, a lack of experimental evidence for strain-induced bandgap-engineered optoelectronic devices at telecommunication wavelengths, which are needed to assess the potential of this class of materials as building blocks for the future integrated photonic platform.

An integral device for photonic circuitry that supports a plethora of applications—such as sensing, data communication and general signal processing—is a monolithically integrated photodetector operating at near-infrared[13–16]. The 1,550 nm wavelength is a prominent spectral choice as it (1) overlaps with the gain spectrum of erbium-doped fibre amplifiers and (2) is transparent for foundry-based silicon photonics. Current state-of-the-art near-infrared photodetectors utilize InGaAs, InP and germanium due to their high absorption (>90%) at telecommunication wavelengths[17–19]. However, III–V materials are not compatible with silicon complementary metal–oxide–semiconductor technology due to the complexity of growth, wafer bonding issues and thermal budget. On the other hand, germanium photodetectors typically show higher noise due to the presence of defects and a dislocation centre at the Si–Ge interface during the epitaxial growth process[20]. By contrast, heterogeneous integration of 2D materials with photonic platforms bears several advantages including strong exciton binding energy, unity-strong index tunability and complementary metal–oxide–semiconductor compatibility due to no lattice-matching requirements (weakly bonded van der Waals forces)[21–27]. Graphene-based integrated photodetectors, although functional, face a fundamental obstacle to achieve low dark current due to their gapless band structure when operated in the photoconductive mode[23]. On the other hand, black phosphorus, a 2D nanocrystal of phosphorus, shows high responsivity and low dark current at 1,550 nm (ref. [21]); however, low stability under ambient conditions limits its application[28].

Our focus therefore is to investigate the effect of induced strain in 2D materials with local strain mapping, which allows for insights into light–matter interaction and enables an additional control knob for device engineering that has not been combined with integrated optoelectronics previously. In this work we demonstrate a strain-engineered photodetector that heterogeneously integrates a multilayer 2H-$MoTe_2$ crystal flake atop a silicon microring resonator (MRR). Our device exhibits spatially varying

[1]Department of Electrical and Computer Engineering, George Washington University, Washington DC, USA. [2]Department of Mechanical and Aerospace Engineering, George Washington University, Washington DC, USA. [3]Department of Electrical and Computer Engineering, University of Minnesota, Minneapolis, MN, USA. [4]Department of Electrical and Computer Engineering, University of Texas, Austin, TX, USA. [5]Department of Information Technology, Ghent University—IMEC, Gent, Belgium. [6]Department of Materials Science and Engineering, University of Pennsylvania, Philadelphia, PA, USA. ✉e-mail: sorger@gwu.edu

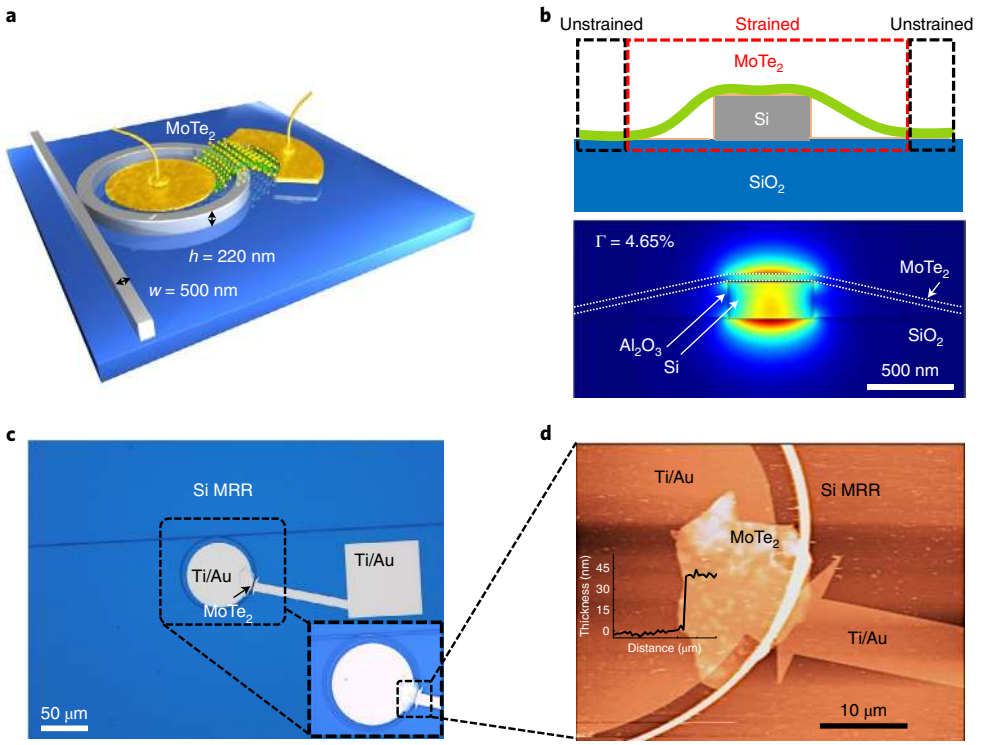

Fig. 1 | MRR-integrated photodetector. a, A schematic of an MRR-integrated $MoTe_2$ photodetector (radius 40 μm, height (*h*) 220 nm, width (*w*) 500 nm). **b**, A schematic of a bent 2D nanocrystal ($MoTe_2$) atop a non-planarized waveguide, which introduces strong localized strain on top of, and in close vicinity to, the waveguide (red dashed box), whereas the flakes away from the waveguide are unstrained (black dashed boxes). A simulated mode profile for a $MoTe_2$-integrated waveguide for a transverse magnetic mode is shown below, in which the cross-sectional structure is extracted from an AFM micrograph. **c**, An optical micrograph of the device (top view), where a few layers of $MoTe_2$ nanocrystals are integrated with a non-planarized silicon MRR (with a spacing layer of ~10-nm-thick Al_2O_3) by using a 2D printer technique[33]. Ti/Au was deposited as electrical contact pads on both sides of the ring resonator to facilitate efficient collection of photogenerated charge carriers. **d**, AFM topography of the active device area in **c**, showing the thickness of the flakes ~40 nm. The inset shows the height profile.

strain, thus resulting in a graded bandgap 2D material photodetector at the photonic-integrated-circuit-relevant wavelength of 1,550 nm. Intentionally wrapping a $MoTe_2$ nanocrystal around a non-planarized waveguide induces local tensile strain overlapping with the waveguide's optical mode. We measure a photoresponsivity of 10 mA W^{-1} (40 nm thick) and 0.5 A W^{-1} (60 nm thick) at −2 V. The device exhibits a low dark current of just 13 nA, a noise equivalent power (NEP) of 90 pW $Hz^{-0.5}$ and operates at frequencies up to ~35 MHz. Such strain-engineered photodetectors using 2D materials integrated with established photonic platforms could potentially open up a new class of optoelectronic components.

Results and discussion

Continuous tuning of physical properties by controlling the mechanical deformation (through strain, for example) offers possibilities for appreciably modifying both the electronic and photonic properties of 2D materials[29,30]. Here, our approach is to exploit strong local uniaxial strain to reduce the optical bandgap of multilayer $MoTe_2$ nanocrystals that are cointegrated with silicon photonic waveguide-based structures. As an example, we show that such a set-up enables photodetection at the technologically relevant wavelength of 1,550 nm (Fig. 1). Bulk $MoTe_2$ is an indirect gap semiconductor with a bandgap of 1.04 eV, where the conduction band minimum lies along the K–Γ symmetry line and the valence band maximum is located at the K-point. Naturally, pristine multilayer (unstrained) $MoTe_2$ is associated with low sub-bandgap absorption at 1,550 nm that results in low photo responsivity of only a few milliamperes per watt due to a roll-off in the absorption edge[31], as demonstrated by a flat $MoTe_2$ atop a planarized waveguide (Supplementary Section 6 and Supplementary Fig. 5). However, intentionally wrapping the 2D film around a non-planarized waveguide with a height of ~220 nm induces a localized tensile strain near the waveguide (Fig. 1a,b). Fundamentally, the performance of 2D-material-based photonic devices is determined by the ability of the optical waveguide mode to interact with the 2D nanocrystal. One typical approach to circumvent this limitation is to place the 2D film onto a planar waveguide and evanescently couple it to the optical mode so that the optical interaction length is not only dictated by the thickness of the 2D film, but also by its longitudinal length[32]. However, such brute-force device engineering results in sizable device footprints, thus negatively impacting the performance of the electrical device, for example, the energy-per-bit efficiency and resistor–capacitor response time, which are both adversely affected by increased electrical capacitance. To reduce the footprint and improve electrical performance, here, we integrate 2D nanocrystals with MRRs, thus increasing the weak light–matter interaction (Fig. 1).

Images of the device illustrate the precise placement capability of the exfoliated $MoTe_2$ flakes—which is enabled by utilizing our in-house-developed 2D material printer technique (Fig. 1c,d, Supplementary Sections 1 and 2, and Supplementary Fig. 1)[33]—atop a thin (10 nm) Al_2O_3 layer that acts as an electrical isolation layer between the silicon-on-insulator photonic chip and the 2D $MoTe_2$ nanocrystal. The optical mode at 1,550 nm (Fig. 1b) couples with the $MoTe_2$ layer through the evanescent field, leading to optical absorption and the creation of photogenerated carriers, which will be collected by the two metal electrodes that are made of both titanium (thickness 5 nm) and gold (thickness 45 nm), which are contacted on opposite sides of the MRR (Fig. 1c). The channel length of this

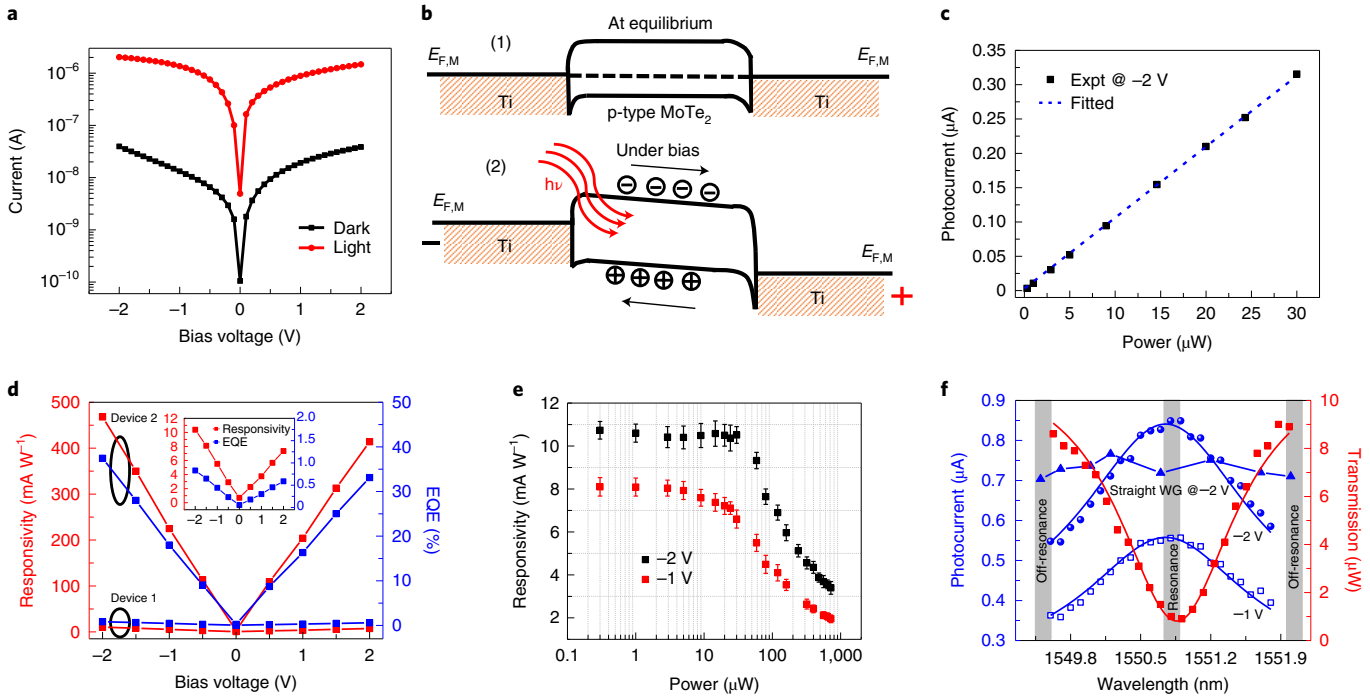

Fig. 2 | Photoresponse of the Au/$MoTe_2$/Au integrated on MRR. a, Typical *I*–*V* characteristics (semi-logarithmic plot) of the Au/$MoTe_2$/Au diode showing around two orders of magnitude enhancement for light (red) over dark (black) conditions. **b**, A schematic energy band diagram explains the photodetection mechanism under the equilibrium state (1) and under bias (2), showing the flow of charge carriers on excitation. $E_{F,M}$ denotes the Fermi level of the metal. **c**, Photocurrent versus incident optical power, showing the responsivity (~10.3 mA W^{-1}) of the device at −2 V. **d**, The responsivity and EQE as a function of bias voltage for two devices (device 1 thickness 40 nm, coverage length 15 μm; device 2 thickness 60 nm, coverage length 30.7 μm), showing symmetric linear variation due to M–S–M device configurations. The inset shows the magnified responsivity and EQE plots for device 1. **e**, The responsivity of the Au/$MoTe_2$/Au detector as a function of illuminated optical power for −1 V and −2 V, respectively. **f**, The spectral response of the MRR-integrated photodetector, showing maximum responsivity at the resonance wavelength (1,550.75 nm) for −1 V (open squares) and −2 V (closed spheres) when the optical transmission (closed red squares) is at its minimum. A photodetector showing ~50% photocurrent enhancement compared with off-resonant conditions (1,549.65 nm). The spectral response of $MoTe_2$-integrated non-planarized straight (not MRR) waveguide (WG) is shown (blue closed triangles) as a reference.

$MoTe_2$ two-terminal photodetector is ~800 nm (with a waveguide width of ~500 nm), where one of the electrical contacts is positioned ~100 nm away from the edge of the ring resonator to create a lateral metal–semiconductor–metal (M–S–M) junction that overlaps with the waveguide mode (Fig. 1b). Two exemplary devices with different dimensions of the 2D material (the coverage length and thickness of the transferred flakes are 15 and 31 μm for device 1, and 40 and 60 nm for device 2) atop of ring resonator are discussed below (Fig. 1d).

A representative current–voltage (*I*–*V*) curve shows efficient photodetection, as indicated by the 100:1 photocurrent to dark current ratio at −1 V bias (Fig. 2a). The device is associated with a low dark current of ~13 nA at −1 V bias, which is around two to three orders lower than graphene and about two times lower than graphene-contacted transition metal dichalcogenide photodetectors, respectively[26,27] (Supplementary Section 12 and Supplementary Table 1). The symmetric nature of the *I*–*V* curve indicates the formation of two back-to-back (Ti/$MoTe_2$) Schottky junctions. The working principle of this detector is photocarrier generation across the bandgap, where the applied voltage bias across the two-terminal contacts enables charge carrier separation (Fig. 2b). The work function (4.3 eV) of titanium at equilibrium ensures Fermi-level alignment with the p-doped $MoTe_2$ (ref. [26]) (Fig. 2b, (1)). The formation of the Schottky barrier at the junction suppresses carrier transport, thus resulting in low dark current. With bias voltage applied, the potential drop across the junction reduces the height of the Schottky barrier (Fig. 2b, (2)). Following illumination from the laser source, the generated photocarriers are separated due to the formation of a built-in potential inside the junction, resulting in photocurrent. We test the response of the detector as a function of the waveguide input power and bias voltage to obtain the photoresponsivity (Fig. 2c,d). After calibrating for coupling losses (Supplementary Section 11 and Supplementary Fig. 14), we find an external responsivity (that is, I_{photo}/P_{input}) of 10 and 468 mA W^{-1} at −2 V for devices 1 and 2, respectively, which is 1.75 times higher than a waveguide-integrated $MoTe_2$ detector tested at 1,310 nm (ref. [26]) (Supplementary Section 12 and Supplementary Table 1). The high responsivity of these $MoTe_2$ detectors operating at 1,550 nm can be attributed to enhanced absorption from (1) the strain-engineered lowered bandgap and (2) the MRR photon lifetime enhancement proportional to the finesse of the cavity (Supplementary Section 3 and Supplementary Fig. 2). The responsivity varies linearly as a function of bias voltage—corresponding to a back-to-back (M–S–M) junction—and shows that the device is not yet driven into saturable absorption at these power levels (Fig. 2c,d). The external quantum efficiency (EQE) can be determined by $EQE = R \times hc/q\lambda$, where, R, h, c, q and λ are the responsivity, Planck's constant, speed of light in vacuum, elementary electron charge and operating wavelength, respectively. The EQEs are 1% and 37% at −2 V for devices 1 and 2, respectively (Fig. 2d). The variation in responsivity as a function of the optical input power shows a flat response until $P_{input} = 30$ μW, where state-filling blockage sets in as the generation of excess carriers increases the radiative recombination for higher power (P_{input}) in the waveguide (Fig. 2e). We first consider the impact of the MRR on the

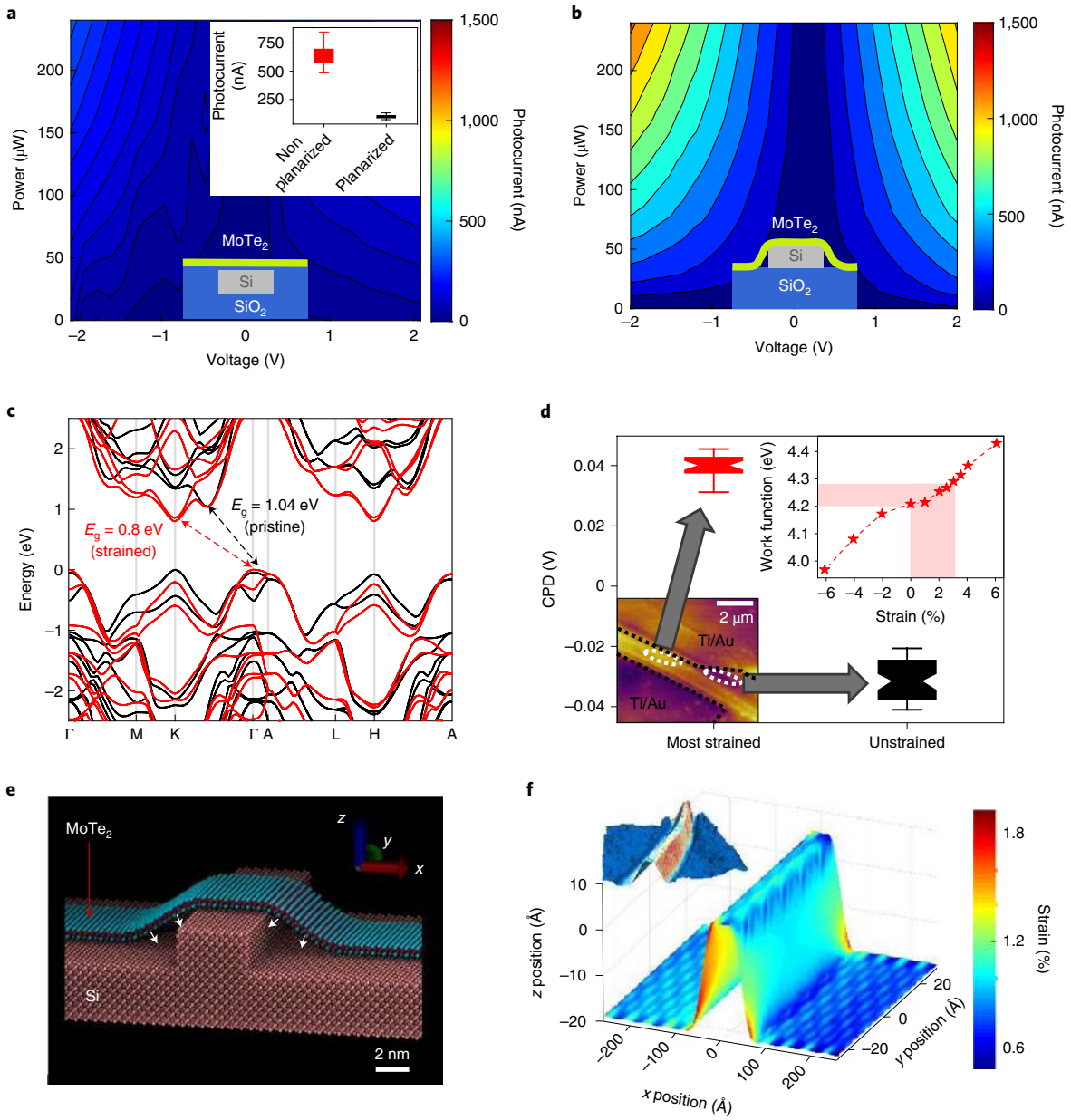

Fig. 3 | Mechanism of enhanced photocurrent. a,**b**, The measured photocurrent as a function of incident light power and electric bias at room temperature for a planarized (**a**) and non-planarized (**b**) $MoTe_2$ photodetector at 1,550 nm. The schematics of the photodetectors are shown in the insets at the bottom. The inset at the top right of **a** is a boxplot of the waveguide-integrated photodetector for planarized and non-planarized geometries for multiple (11) devices, where the lateral dimensions and thicknesses range from 10 to 20 μm and 40 to 60 nm, respectively. **c**, Bulk band-structure calculations obtained by DFT calculations of pristine (black) and 4% strained (red) $MoTe_2$, showing a reduced bandgap. The valence band maximum is set to zero. **d**, A boxplot of the CPD obtained through KPFM for device 1, for the most strained region (red), along the edge of the waveguide and unstrained region (black) and away from the waveguide (marked with white dotted ovals on the CPD image in the bottom-left inset). The ends of the box are the upper and lower quartiles and the whiskers extend to the highest and lowest observations. The change in work function is attributed to the strain imparted by the waveguide on the $MoTe_2$ flakes. The metallic (Ti/Au) contact near the waveguide is marked with black dotted lines in the bottom-left inset. The upper-right inset shows the work function versus the strain trend calculated from DFT. Negative and positive strain values correspond to compressive and tensile strain, respectively. The red shaded region overlays the KPFM-obtained work function variation in a non-planarized device showing the corresponding range of strain. **e**, An exemplary 100:1 aspect-ratio-locked model obtained by molecular dynamics simulations for monolayer $MoTe_2$ after energy minimization. The strain is generated by (attractive) van der Waals forces between the suspended monolayer and the substrate (as indicated by the white arrows). **f**, The strain map variation of the model shown in **e**, calculated on the basis of the atomic position changes of the central molybdenum layer, showing maximum strain on the corners and edges of the waveguide and on the suspended section. The inset is a map of the work function (from CPD KPFM) of the strained flakes (device 2) overlaid on topography, showing similar local variations across the waveguide.

detector's performance. When operated at a fixed power of 120 μW at different bias voltages, we find a ~50% enhanced photocurrent ON (versus OFF) resonance, which matches the MRR's finesse of ~1.6 (Fig. 2f and Supplementary Section 4 and Supplementary Fig. 3). However, the MRR-integrated $MoTe_2$ photodetector exhibits ~1.2-fold enhancement of the photocurrent at 1,550.75 nm (ON

resonance) in comparison with the straight waveguide photodetector (non-planarized) (Fig. 2f, Supplementary Section 5 and Supplementary Fig. 4). We note that although an MRR with a higher finesse will improve responsivity, it can reduce the 3 dB response speed of the detector due to a longer photon cavity lifetime if the latter is the limiting factor and not the carrier lifetimes (that is, relating to the gain-bandwidth product figure of merit of photodetectors).

Strain-induced modulation of the electronic bandgap in 2D semiconductors wrapped around a patterned substrate has previously been observed[34]. Our experimental observation of the enhanced photocurrent for the wrapped-around detector versus the planarized control sample might have also benefited from the induced strains (Fig. 3a,b, Supplementary Section 6 and Supplementary Fig. 5). By using first-principles density functional theory (DFT) for monolayer $MoTe_2$, our calculated band structures suggested that the electronic gap acquired a red-shift with tensile strains, potentially bridging the electronic gap with the telecommunication wavelength (Supplementary Section 9 and Supplementary Fig. 12b). Subject to higher tensile strain, we note that the valence bands shift towards higher energies (at Γ). Furthermore, the conduction bands at the K- and H-points shift towards lower energies and become the conduction band minimum with equal energies (Fig. 3c). As a result, the bandgap reduces from about 1.04 eV for pristine to about 0.8 eV for strained $MoTe_2$ (4%), yet the material remains an indirect bandgap semiconductor (Fig. 3c). Several studies on strain-induced modulation of the band structure for 2D materials have relied on DFT to accurately explain the variation of the bandgap obtained in the experiments[12,35–37], thus supporting our observed results. However, in our case, this strain varies spatially and creates a graded bandgap (rather than a unique bandgap across the entire structure) of 0.8 eV; therefore, the bandgap (E_g) does not end abruptly at 0.8 eV. These results together suggest that tensile strain can open up interband optical transitions at the telecom frequency, which are otherwise forbidden in the unstrained case. These are consistent with our observed experimental findings of an enhanced photoresponse at 1,550 nm for strained (versus pristine) photodetectors discussed above (Fig. 3a,b).

To obtain a deeper understanding of strain-induced band structure modulation, we performed Kelvin probe force microscopy (KPFM), which measured the local contact potential difference (CPD) between the 2D nanocrystal and an atomic force microscopy (AFM) probe with nanometric spatial resolution[38]. The local work function of the 2D nanocrystal can be derived from the CPD using the relation $V_{CPD} = \frac{\phi_{tip} - \phi_{sample}}{-e}$, where ϕ_{tip} and ϕ_{sample} are the work functions of the tip and sample, respectively, and e is the electronic charge[38]. This scanning probe microscopy technique offers advantages over commonly used optical measurement techniques, including Raman and photoluminescence spectroscopy[11,12,34,35], due to nanometre (subdiffraction-limited) probe area, and is thus able to collect local information on the electronic structure of the material. The KPFM box plot of device 1 (Fig. 3d) shows a discernible increase in work function near the waveguide compared with the flat and unstrained regions. The increment in the work function of $MoTe_2$ (Δwork function ≈ 0.08 eV) corresponds to a change of ~3% tensile strain as calculated by DFT (Fig. 3d, inset). The mismatch in the absolute value of the work function of the material (calculated by DFT and obtained from KPFM) can be attributed to the nature of DFT calculations where $MoTe_2$ is in its isolated form, without considering the effects of the substrates and environment[39,40]. A similar work function change induced by strain and its detection by KPFM is reported for WS_2 and graphene[39,41]. Every measurement approach bears a degree of uncertainty, as does the strain-determination technique for the submicrometre-integrated device cross-correlating KPFM and DFT results. Note that substrate charging effects (trapped charges) can be ruled out as the origin of the observed difference in CPD at, versus off, the waveguide due to the strain-induced modulation of the work function for multiple devices with different geometries (Supplementary Section 8 and Supplementary Fig. 10). As all of the measurements were carried out in the same environment, with the same experimental set-up and on the chip(s) made of same underlying substrate (SiO_2), the effect of dielectric medium can be neglected/normalized from the comparison of the strained (non-planarized) and unstrained (planarized) devices (Supplementary Section 8 and Supplementary Fig. 11). Furthermore, the Δwork function (top of the waveguide – away from the waveguide) values in the same device are of utmost interest to us when estimating the amount of induced strain. Given the consistencies, and the plurality of the measurement and support approaches, we mainly attribute the higher variability in the strained devices to the different amount of strain generated in the material due to different waveguide geometry.

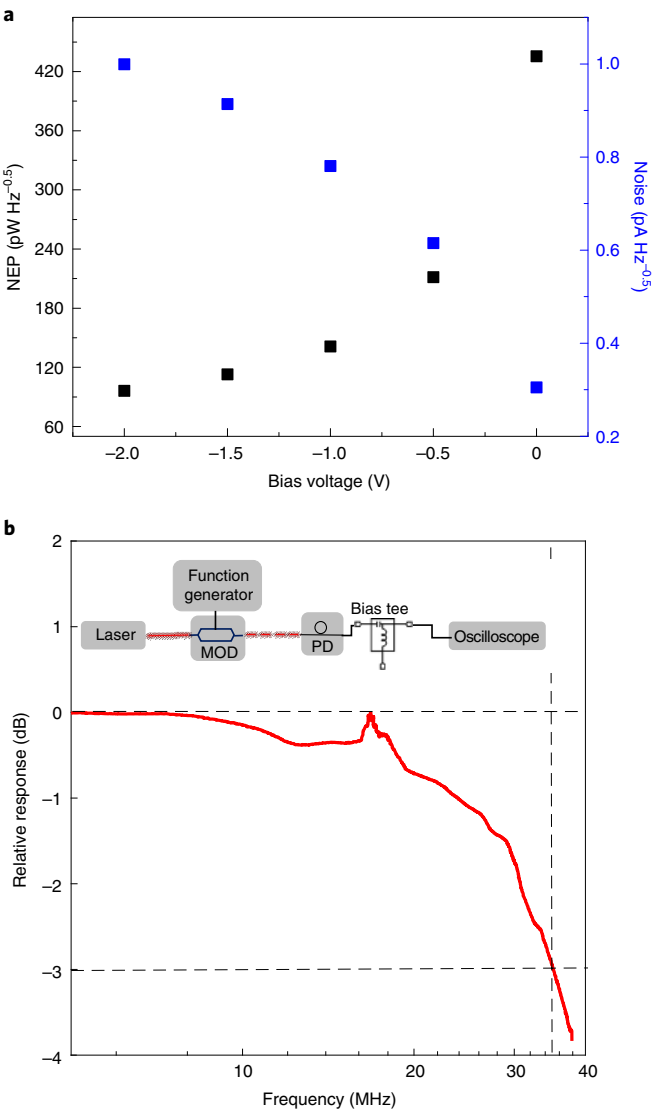

Fig. 4 | Dynamic performance. a, The device is operating in the photoconductive mode, showing a low dark current that leads to a low NEP value of 90 pW Hz$^{-0.5}$ at 2 V. **b**, The alternating current photoresponse as a function of the modulated frequency of light signal showing a 3 dB cutoff frequency of 35 MHz, which is mainly limited by low transit time. The inset shows the dynamic response measurement set-up. MOD and PD refer to the modulator and photodetector (that is, the device-under-test, DUT), respectively.

To better approximate the amount of strain, we performed several supporting experiments that revealed the local strain in our devices to be about 3 ± 1% (Supplementary Section 9 and Supplementary Fig. 12). We can claim a more specific value of the strain for submicrometre-integrated devices only when we can develop a more direct way to map the strain for the nanostructures. We performed molecular dynamics simulations of a structure that is geometrically similar to the original device to demonstrate the strain-generation mechanism in the material due to device geometry (for example, with an aspect ratio of 100:1) for computational tractability (Fig. 3e and details in Supplementary Section 7). Comparing the atomic positions in the $MoTe_2$ monolayer before and after energy minimization of the structure yields strains in the suspended region and on the edges of the waveguide (along the tensile direction within the monolayer). The strain is generated by (attractive) van der Waals forces between the suspended monolayer and the substrate, whereby it is favourable for the monolayer to stretch slightly in the entire suspended region to allow a larger portion of its distal ends to remain closer to the substrate. This miniaturized calculation is not expected to quantitatively reproduce the strain for the full-size device precisely as (1) the region of favourable van der Waals interactions in the simulation is small (these interactions decay rapidly with distance anyway) and (2) the separation between the monolayer and the substrate in the miniaturized structure increases rapidly away from the distal ends. Nevertheless, the simulation does correctly illustrate the mechanism of strain generation. Figure 3f overlays the calculated strain on the basis of the positions of the rows of atoms in the centre of the molybdenum strip (which are considered to be the most representative for strain calculations) on the monolayer geometry to depict concentrated strain in the suspended section and on the edges, which displays a qualitatively similar trend to the KPFM result (Fig. 3f, inset) and supports the device-observed strain-dependent tuning of the work function of the 2D material.

To understand the detection limit of the device, we determine the NEP, that is, the amount of incident light power that generates a photocurrent equal to the noise current (NEP = i_n/R, where, i_n is noise current and R is the responsivity). There are mainly two sources of noise at high signal speeds, the shot noise ($\sqrt{2qI_d}$) and Johnson noise ($\sqrt{\frac{4k_BT}{R_{sh}}}$), which contribute to the total noise current. However, for a photodetector operating at a photoconducting mode, the shot noise normally dominates the Johnson noise. Here, the NEP is found to be ~90 pW $Hz^{-0.5}$, which is the lowest among the devices, although device 2 shows higher responsivity (high dark current), thus revealing the trade-off between the sensitivity and noise current. However, our device exhibits around two orders higher sensitivity than the graphene/silicon photodetector[42] due to lower dark current when operating in the photoconductive mode, and comparable sensitivity to NEP as black phosphorus photodetectors[43]. The variation of NEP shows a gradual decrease for higher bias voltages (Fig. 4a), enabling low-light-level sensing, which can be further improved by the formation of a p–n junction.

We test the dynamic response of the detector using a modulated laser input (Fig. 4b). The modulated optical output is coupled into the device where the electrical output was measured through a radio frequency microwave probe and the normalized frequency response was analysed via the S_{21} parameter of the network analyser (Fig. 4b). Our photodetector device displays a 3 dB bandwidth of 35.6 MHz at 2 V. The response time of a cavity-integrated photodetector is mainly governed by these three factors: the carrier transit time (τ_{tr}), charge/discharge time of the junction capacitance (τ_{RC}) and photon lifetime (τ_{cav}). Hence, the temporal response of the detector is determined by $\tau_R = \sqrt{(\tau_{tr}^2 + \tau_{RC}^2 + \tau_{cav}^2)}$. Here, the transit time is given by $\tau_{tr} = l^2/2\mu V_{bias}$, where l is the channel length of the $MoTe_2$ detector and μ is the carrier mobility. From this top-gated configuration, when the 2D nanocrystal is atop the waveguide, the field-effect mobility is 1.2 $cm^2 V^{-1} s^{-1}$ (Supplementary Section 10 and Supplementary Fig. 13). With a channel length of 0.8 µm, the transit time is found to be 3.2 ns ($f_{3dB\text{-estimated}} \approx 49.7$ MHz) and the main limiting factor.

Conclusions

We demonstrate a strain-induced absorption-enhanced 2D nanocrystal ($MoTe_2$)-based silicon photonic microring-integrated photodetector featuring high responsivity of 0.01 A W^{-1} (device 1) and ~0.5 A W^{-1} (device 2) at 1,550 nm, with a low NEP of 90 pW $Hz^{-0.5}$. Subject to mechanical strain, the bandgap shifts towards 0.80 eV for strained $MoTe_2$, when the 2D nanocrystal is wrapped around a non-planarized silicon waveguide. The local enhancement of the work function mapped out by KPFM corresponds to a local change of strain of ~3 ± 1% according to DFT calculations. The device responsivity can be further improved using a high-quality-factor (Q) cavity resonator. We observe a 3 dB bandwidth of 35 MHz, where the response time is transit time limited. This strain-engineered bandgap enables optical absorption at 1,550 nm, resulting in an integrated photonic detector that could potentially open up a new pathway for future on-chip photonic circuits.

Online content

Any methods, additional references, Nature Research reporting summaries, source data, extended data, supplementary information, acknowledgements, peer review information; details of author contributions and competing interests; and statements of data and code availability are available at https://doi.org/10.1038/s41566-020-0647-4.

Received: 12 November 2019; Accepted: 12 May 2020;
Published online: 22 June 2020

References

1. Jacobsen, R. S. et al. Strained silicon as a new electro-optic material. *Nature* **441**, 199–202 (2006).
2. Cheng, T.-H. et al. Strain-enhanced photoluminescence from Ge direct transition. *Appl. Phys. Lett.* **96**, 211108 (2010).
3. Feng, J., Qian, X., Huang, C.-W. & Li, J. Strain-engineered artificial atom as a broad-spectrum solar energy funnel. *Nat. Photon.* **6**, 866–872 (2012).
4. Lee, M. L., Fitzgerald, E. A., Bulsara, M. T., Currie, M. T. & Lochtefeld, A. Strained Si, SiGe, and Ge channels for high-mobility metal-oxide-semiconductor field-effect transistors. *J. Appl. Phys.* **97**, 11101 (2005).
5. Yun, W. S., Han, S. W., Hong, S. C., Kim, I. G. & Lee, J. D. Thickness and strain effects on electronic structures of transition metal dichalcogenides: 2H-MX_2 semiconductors (M = Mo, W; X = S, Se, Te). *Phys. Rev. B* **85**, 1–5 (2012).
6. He, K., Poole, C., Mak, K. F. & Shan, J. Experimental demonstration of continuous electronic structure tuning via strain in atomically thin MoS_2. *Nano Lett.* **13**, 2931–2936 (2013).
7. Yue, Q. et al. Mechanical and electronic properties of monolayer MoS_2 under elastic strain. *Phys. Lett. A* **376**, 1166–1170 (2012).
8. Ghorbani-Asl, M., Borini, S., Kuc, A. & Heine, T. Strain-dependent modulation of conductivity in single-layer transition-metal dichalcogenides. *Phys. Rev. B* **87**, 1–6 (2013).
9. Shi, H., Pan, H., Zhang, Y. W. & Yakobson, B. I. Quasiparticle band structures and optical properties of strained monolayer MoS_2 and WS2. *Phys. Rev. B* **87**, 1–8 (2013).
10. Manzeli, S., Allain, A., Ghadimi, A. & Kis, A. Piezoresistivity and strain-induced band gap tuning in atomically thin MoS_2. *Nano Lett.* **15**, 5330–5335 (2015).
11. Castellanos-Gomez, A. et al. Local strain engineering in atomically thin MoS_2. *Nano Lett.* **13**, 5361–5366 (2013).
12. Aslan, O. B. et al. Probing the optical properties and strain-tuning of ultrathin $Mo_{1-x}W_xTe_2$. *Nano Lett.* **18**, 2485–2491 (2018).
13. Eng, P. C., Song, S. & Ping, B. State-of-the-art photodetectors for optoelectronic integration at telecommunication wavelength. *Nanophotonics* **4**, 277–302 (2015).
14. Feng, B. et al. All-Si photodetectors with a resonant cavity for near-infrared polarimetric detection. *Nanoscale Res. Lett.* **14**, 39 (2019).

15. Walden, R. H. A review of recent progress in InP-based optoelectronic integrated circuit receiver front-ends. In *GaAs IC Symposium IEEE Gallium Arsenide Integrated Circuit Symposium. 18th Annual Technical Digest* 255–257 (IEEE, 1996).
16. Narayana, V. K., Sun, S., Badawy, A.-H., Sorger, V. J. & El-Ghazawi, T. MorphoNoC: exploring the design space of a configurable hybrid NoC using nanophotonics. *Microprocess. Microsyst.* **50**, 113–126 (2017).
17. Liu, K., Sun, S., Majumdar, A. & Sorger, V. J. Fundamental scaling laws in nanophotonics. *Sci. Rep.* **6**, 37419 (2016).
18. Michel, J., Liu, J. & Kimerling, L. C. High-performance Ge-on-Si photodetectors. *Nat. Photon.* **4**, 527 (2010).
19. Goykhman, I., Desiatov, B., Khurgin, J., Shappir, J. & Levy, U. Waveguide based compact silicon Schottky photodetector with enhanced responsivity in the telecom spectral band. *Opt. Express* **20**, 28594 (2012).
20. Wang, J. & Lee, S. Ge-photodetectors for Si-based optoelectronic integration. *Sensors* **11**, 696–718 (2011).
21. Youngblood, N., Chen, C., Koester, S. J. & Li, M. Waveguide-integrated black phosphorus photodetector with high responsivity and low dark current. *Nat. Photon.* **9**, 247–252 (2015).
22. Bie, Y. Q. et al. A $MoTe_2$-based light-emitting diode and photodetector for silicon photonic integrated circuits. *Nat. Nanotechnol.* **12**, 1124–1129 (2017).
23. Octon, T. J., Nagareddy, V. K., Russo, S., Craciun, M. F. & Wright, C. D. Fast high-responsivity few-layer $MoTe_2$ photodetectors. *Adv. Opt. Mater.* **4**, 1750–1754 (2016).
24. Youngblood, N., & Li, Mo. Integration of 2D materials on a silicon photonics platform for optoelectronics applications. *Nanophotonics* **6**, 1205 (2017).
25. Ma, P. et al. Fast $MoTe_2$ waveguide photodetector with high sensitivity at telecommunication wavelengths. *ACS Photonics* **5**, 1846–1852 (2018).
26. Gan, X. et al. Chip-integrated ultrafast graphene photodetector with high responsivity. *Nat. Photon.* **7**, 883–887 (2013).
27. Schuler, S. et al. Controlled generation of a p–n junction in a waveguide integrated graphene photodetector. *Nano Lett.* **16**, 7107–7112 (2016).
28. Island, J. O., Steele, G. A., van der Zant, H. S. J. & Castellanos-Gomez, A. Environmental instability of few-layer black phosphorus. *2D Mater.* **2**, 11002 (2015).
29. Deng, S., Sumant, A. V. & Berry, V. Strain engineering in two-dimensional nanomaterials beyond graphene. *Nano Today* **22**, 14–35 (2018).
30. Johari, P. & Shenoy, V. B. Tuning the electronic properties of semiconducting transition metal dichalcogenides by applying mechanical strains. *ACS Nano* **6**, 5449–5456 (2012).
31. Keum, D. H. et al. Bandgap opening in few-layered monoclinic $MoTe_2$. *Nat. Phys.* **11**, 482–486 (2015).
32. Shiue, R.-J. et al. High-responsivity graphene–boron nitride photodetector and autocorrelator in a silicon photonic integrated circuit. *Nano Lett.* **15**, 7288–7293 (2015).
33. Hemnani, R. A. et al. Towards a 2D printer: a deterministic cross contamination-free transfer method for atomically layered material. *2D Mater* **6**, 015006 (2018).
34. Li, H. et al. Optoelectronic crystal of artificial atoms in strain-textured molybdenum disulphide. *Nat. Commun.* **6**, 7381 (2015).
35. Conley, H. J. et al. Bandgap engineering of strained monolayer and bilayer MoS_2. *Nano Lett.* **13**, 3626–3630 (2013).
36. Frisenda, R. et al. Biaxial strain tuning of the optical properties of single-layer transition metal dichalcogenides, *npj 2D Mater. Appl.* **1**, 10 (2017).
37. Desai, S. B. et al. Strain-induced indirect to direct bandgap transition in multilayer WSe_2. *Nano Lett.* **14**, 4592–4597 (2014).
38. Melitz, W., Shen, J., Kummel, A. C. & Lee, S. Surface science reports kelvin probe force microscopy and its application. *Surf. Sci. Rep.* **66**, 1–27 (2011).
39. Sarwat, S. G. et al. Revealing strain-induced effects in ultrathin heterostructures at the nanoscale. *Nano Lett*. **18**, 2467–2474 (2018).
40. Jung, D. Y., Yang, S. Y., Park, H., Shin, W. C., Oh, J. G., Cho, B. J. & Choi, S.-Y. Interface engineering for high performance graphene electronic devices. *Nano Converg.* **2**, 11 (2015).
41. Meng, L. et al. Two-dimensional WS_2 lateral heterojunctions by strain modulation. *Appl. Phys. Lett.* **108**, 263104 (2016).
42. Casalino, M. et al. Vertically illuminated, resonant cavity enhanced, graphene–silicon Schottky photodetectors. *ACS Nano* **11**, 10955–10963 (2017).
43. Huang, L. et al. Waveguide-integrated black phosphorus photodetector for mid-infrared applications. *ACS Nano* **13**, 913–921 (2019).

Methods

DFT study. DFT calculations were performed as implemented in the Vienna ab initio simulation package[44]. The exchange correlation energy is described by the generalized gradient approximation using the Perdew–Burke–Ernzerhof functionals[45]. As DFT usually underestimates the bandgap of semiconductors, we used the HSE06 hybrid functional[46] for the exchange-correlation term, which provides reliable results for bandgaps. The plane-wave cutoff energy was set to 300 eV. Spin-orbit coupling was taken into consideration. The bulk crystal structure was relaxed until the total energy converged to 10^{-6} eV and the Hellmann–Feynman force on each atom was less than 0.001 eV $Å^{-1}$. For relaxation, the Brillouin zone was sampled using a Monkhorst-pack $21\times21\times21$ grid[47]. The optimized lattice parameters for the pristine bulk structure in the 2H phase are $a=3.52$ Å and $c=13.97$ Å. To calculate work functions, a large vacuum spacing of 30 Å was added along the stacking (out-of-plane) direction. We then tracked the plane-averaged electrostatic potential into the vacuum, where the vacuum energy is usually reached within a few ångstroms of the surface. The work function is therefore obtained by subtracting the mid-gap energy from the vacuum energy. Here we used the mid-gap energy instead of Fermi energy, as Fermi energy is a quantity that varies with doping and also can be anywhere in the band gap for our cases.

Device fabrication. Photonic integrated circuits were processed in silicon photonics (including the MRRs) using silicon on the insulator (epitaxial Si layer 220 nm, buried oxide layer 2 µm). Devices were patterned with electron-beam lithography using a negative resist ARN 7520. The patterned features were etched with inductively coupled plasma. The photoresist mask was removed using acetone wash and short oxygen plasma cleaning. The samples were cleaned using acetone followed by isopropanol and subsequently dried using nitrogen gas. The sample was heated on a hot plate for 2–3 mins at 180 °C for better adhesion of the flakes. The few-layered $MoTe_2$ flakes were transferred onto the MRR using a 2D printer[33]. After the transfer process, a thin layer of poly(methyl methacrylate) (~300 nm) was spin coated on the sample at 1,500 r.p.m. and followed by a post-baked process at 180 °C for 2 min. For electrical characterization, the metal contact pads (80×80 µm^2) were patterned using an electron-beam lithography process. The samples were then developed in methyl isobutyl ketone:isopropanol (3:1) solution. After development, a mild oxygen plasma was applied to clean the poly(methyl methacrylate) residues on the exposed 2D layer. A thin layer of titanium (5 nm) and gold (45 nm) was deposited using an electron beam evaporation process followed by lift-off in acetone. Details of the step-by-step fabrication process flow can be found in Supplementary Section 1 and Supplementary Fig. 1.

Device measurement. To measure the responsivity of the device, we coupled 1,550 nm continuous-wave input laser (Agilent 8164B) and detected the photocurrent through a source meter (Keithly 2600B). Here, P_{input} is the power reaching the MRR-$MoTe_2$ detector, which was estimated by considering the input grating coupler coupling loss and the silicon waveguide transmission loss (Supplementary Section 11 and Supplementary Fig. 14). The spectral response of the MRR-integrated device was measured using a broadband laser (AEDFA-PA-30-B-FA) injected into the grating coupler optimized for the transverse magnetic mode propagation. The light output from the MRR was coupled to the output fibre and detected by the optical spectral analyser (Thorlabs OSA202). The experimental set-up for measuring the photodetector devices is shown in Supplementary Fig. 14 (Supplementary Section 11) and a ground-source radio frequency probe was used.

KPFM measurement. A scanning probe microscopy technique commonly known as KPFM was exploited to gather local electrical information from the sample. For this study, a commercial AFM, MFP-3D (Asylum Research), was used, along with a BudgetSensors chromium/platinum-conductive-coated probe (Multi75E-G). To calculate the work function of the probe tip, the latter was calibrated by scanning a freshly cleaved highly ordered pyrolytic graphite surface ($\varphi=4.6$ eV) several times and then an average was performed for all of the scans. The scanning was done in the attractive (non-contact) imaging regime to avoid any possible contamination of the AFM tip. The work function of the tip was calculated to be 4.1875 eV. In all measurements, the sample was grounded to avoid the possibility of the surface charge modifying the CPD value.

Molecular dynamics simulation. The molecular dynamics simulations were performed using LAMMPS software (version, 19 September 2019)[48]. Intracrystal interactions in $MoTe_2$ were modelled using the Stillinger–Weber potential (https://lammps.sandia.gov/doc/pair_sw.html)[49,50]. Parameters specific to $MoTe_2$ and initial crystal structures were taken from ref. [51]. Non-bonded Lennard–Jones potential parameters between the silicon substrate and the $MoTe_2$ flake were calculated from ref. [52] through the customary Lorentz–Berthelot mixing rules[52]. The silicon substrate was assumed to be rigid.

Data availability

The data that support the plots within this paper and other findings of this study are available from the corresponding author on reasonable request.

References

44. Kresse, G. & Furthmüller, J. Efficient iterative schemes for *ab initio* total-energy calculations using a plane-wave basis set. *Phys. Rev. B* **54**, 11169–11186 (1996).
45. Perdew, J. P., Burke, K. & Ernzerhof, M. Generalized gradient approximation made simple. *Phys. Rev. Lett.* **77**, 3865–3868 (1996).
46. Paier, J. et al. Screened hybrid density functionals applied to solids. *J. Chem. Phys.* **124**, 154709 (2006).
47. Pack, J. D. & Monkhorst, H. J. "Special points for Brillouin-zone integrations"—a reply. *Phys. Rev. B* **16**, 1748–1749 (1977).
48. Plimpton, S. Fast parallel algorithms for short-range molecular dynamics. *J. Comput. Phys.* **117**, 1–19 (1995).
49. Stillinger, F. H. & Weber, T. A. Computer simulation of local order in condensed phases of silicon. *Phys. Rev. B* **31**, 5262–5271 (1985).
50. Jiang, J.-W. & Zhou, Y.-P. in *Handbook of Stillinger–Weber Potential Parameters for Two-Dimensional Atomic Crystals* (InTech, 2017).
51. Ichimura, M. Stillinger–Weber potentials for III–V compound semiconductors and their application to the critical thickness calculation for InAs/GaAs. *Phys. Status solidi* **153**, 431–437 (1996).
52. Zhou, Y.-P. & Jiang, J.-W. Molecular dynamics simulations for mechanical properties of borophene: parameterization of valence force field model and Stillinger-Weber potential. *Sci. Rep.* **7**, 45516 (2017).

Acknowledgements

V.J.S. is supported by AFOSR (grant no. FA9550-17-1-0377) and ARO (grant no. W911NF-16-2-0194). M.A.S.R.S., B.U. and S.D.S. acknowledge support from the US Department of Energy, Office of Science, Basic Energy Sciences under award no. DE-SC0018041. S.R.B. acknowledges support from NSF grant nos. DMR-1839175 and CCF-1838435. We acknowledge computational support from the Minnesota Supercomputing Institute (MSI).

Author contributions

R.M. and V.J.S. initiated the project and conceived the experiments. C.P. and T.X. fabricated the devices. R.M. and M.A.S.R.S. performed the measurements and data analysis. B.U., S.D.S., J.G.A., T.L., M.M. and R. Amin provided modelling and the theoretical analysis. A.F.B. and S.R.B. performed supporting experiments. D.V.T. provided planarized photonic chip. R.M and V.J.S. co-wrote the manuscript, and R. Agarwal provided suggestions throughout the project. All authors discussed and commented on the manuscript.

Competing interests

The authors declare no competing interests

Additional information

Supplementary information is available for this paper at https://doi.org/10.1038/s41566-020-0647-4.

Correspondence and requests for materials should be addressed to V.J.S.

Reprints and permissions information is available at www.nature.com/reprints.